International Journal of Heat and Mass Transfer 83 (2015) 39–50

Contents lists available at ScienceDirect

International Journal of Heat and Mass Transfer

journal homepage: www.elsevier.com/locate/ijhmt

Study of cellular flow structure and pitchfork bifurcation in a laterally-heated cube

Reui-Kuo Lin [a,1], Wen-Hann Sheu [b,c,*]

[a] Department of Marine Engineering, Taipei College of Maritime Technology, No. 212, Section 9, Yen Ping N. Rd., Shihlin Dist., Taipei 11174, Taiwan
[b] Department of Engineering Science and Ocean Engineering, National Taiwan University, Taiwan
[c] Center of Advanced Study in Theoretical Sciences (CASTS), National Taiwan University, Taiwan

ARTICLE INFO

Article history:
Received 31 January 2013
Received in revised form 21 November 2014
Accepted 24 November 2014
Available online 12 December 2014

Keywords:
Three-dimensional
Nonlinear system
Cellular flow
Pitchfork bifurcation
Hopf bifurcation
Quasi-periodic bifurcation

ABSTRACT

This paper is the continuation of our study of flow development from a motionless conductive state in a thermally driven cavity. A series of complex nonlinear bifurcations was addressed in a three-dimensional partially heated rectangular cavity. Prior to chaos, the dynamic phenomena in the investigated nonlinear system include pitchfork bifurcation, Hopf bifurcation, periodic ultraharmonics, and quasi-periodic bifurcation. In this study the formation of different cellular flow structures and the scenario of pitchfork bifurcation are addressed. The solutions for the incompressible fluid flow investigated at different Rayleigh numbers are computed from the divergence-free compensated solution algorithm and the wavenumber-optimized upwinding scheme for accurately approximating the convection terms. The three-dimensional cellular flow details and the physically meaningful vortical flow insight are extracted to improve our understanding of the change of three-dimensional vortical and cellular flow features with respect to the Rayleigh number in the thermal driven cavity.

1. Introduction

Free convection resulting from a thermally driven buoyancy force may strongly affect product quality in many material processing industries. In the Bénard convection experiment, fluid flow transition from a state of conduction to a state of complex cellular flow has been revealed. In 1916, Lord Rayleigh (1916) [1] interpreted the phenomena found in Bénard experiment by making Boussinesq assumption along the gravitational direction. Application of this assumption amounts to introducing a buoyancy force to the equations of motion along the direction of gravity. He also showed that flow bifurcations of different types set in as the dimensionless Rayleigh numbers exceed their corresponding critical values. After this pioneering work, numerous studies have been performed to investigate this problem; see among others Chandrasekhar [2] and Drazin & Reid [3] for the linear theories, and Kirchgässner [4] and Yudovich [5], and the references therein for the nonlinear theories. Such a buoyancy induced flowfield has also been known to affect semiconductor fabrication in molten materials during crystal growth.

As the characteristic Rayleigh number *Ra* or Grashof number *Gr* exceeds their respective critical respective value, thermal driven flow will undergo different bifurcations such as the Hopf, pitchfork, and turning-point bifurcations. Due to the inevitable flow destabilization and possible solution multiplicity present in the nonlinear flow system, many experimental studies of these two issues have been conducted with the aim to improve design reliability, in addition to cost reduction, for some practical crystal growth processes.

Our objective of analyzing the three-dimensional flow motion due to thermal effect (free convection) is to improve our understanding of the cellular vortex structure and pitchfork bifurcation. This article is organized as follows. In Section 2 the working equations for simulating natural convection flow are presented together with the well-posed initial and boundary conditions. We then apply in Section 3 the computationally effective upwind scheme and the continuity-preserving discretization scheme employed to solve the elliptic–parabolic set of incompressible viscous flow equations in non-staggered grids. Description of the problem and discussion of the results are then given in Section 4. Evolution of a cellular flow with the increase of Rayleigh number in laterally heated cube has been discussed in the result section. We also

* Corresponding author at: Department of Engineering Science and Ocean Engineering, National Taiwan University, Taiwan. Tel.: +886 2 33665746; fax: +886 2 23929885.
E-mail addresses: rklin@mail.tcmt.edu.tw (R.-K. Lin), twhsheu@ntu.edu.tw (W.-H. Sheu).
[1] Tel.: +886 2 28102292x5022; fax: +886 2 28106688.

http://dx.doi.org/10.1016/j.ijheatmasstransfer.2014.11.071
0017-9310/

aim to show that as the Rayleigh number Ra becomes larger than the critical value, the solution of the investigated nonlinear equations will be bifurcated from a symmetric flow to its unsymmetric counterpart flow. For the sake of completeness, the route towards chaos from a flow initially at rest is summarized. The concluding remarks are drawn in the final Section 5.

2. Working equations

Flow transition from a steady state to an oscillatory state depends strongly on the Prandtl number of the fluid and the aspect ratio of the cavity [6]. In this study we investigate both of the vortex flow structure and flow bifurcation in a cubic cavity, within which the fluid has a Prandtl number of 0.71. Under the constant thermal diffusivity condition, laminar flow of an incompressible and Newtonian fluid has been investigated along with the Boussinesq approximation applied to the time-dependent equations of motion along the direction of gravity. The resulting differential equations to be solved in the gravity field $\vec{g} = (0, -g, 0)$ are given below as [7–9]

$$\nabla \cdot \vec{v} = 0, \tag{1}$$

$$\frac{\partial \vec{v}}{\partial t} + (\vec{v} \cdot \nabla)\vec{v} = -\nabla p + Pr\nabla^2 \vec{v} + \vec{F}, \tag{2}$$

$$\frac{\partial T}{\partial t} + (\vec{v} \cdot \nabla)T = \nabla^2 T. \tag{3}$$

The force vector $\vec{F}(\equiv RaPr\,T\vec{e}_y)$ represents the buoyancy force along the gravity direction $\vec{e}_y$. In the above, $Ra(\equiv g\beta(T_h - T_c)L^3/\alpha\nu)$ and $Pr(\equiv \nu/\alpha)$ are known respectively as the Rayleigh and Prandtl numbers.

3. Numerical method

According to the Helmholtz–Hodge decomposition theorem [10], any vector field $\vec{W}$ can be decomposed into a solenoidal field without the normal component along the boundary and a gradient of one scalar function. By choosing the scalar function as p and the divergence-free vector as $\vec{v}$, one can write $\vec{v} = \vec{W} - \nabla p$ based on the underlying decomposition theorem. A projection operator P, which maps the vector $\vec{W}(\equiv \vec{v} + \nabla p)$ onto its divergence-free vector field $\vec{v}$, is defined first. It is then applied to the equation $\vec{v} = \vec{W} - \nabla p$ to get $P\vec{W} = P\vec{v} + P(\nabla p)$. Thanks to the definition of P, the equation $P\vec{W} = P\vec{v} = \vec{v}$ and, in turn, the equation $P(\nabla p) = 0$ are resulted. This is followed by applying the above chosen operator P to both hand sides of the Eq. (2) to get $P\frac{\partial \vec{v}}{\partial t} = P[-(\vec{v} \cdot \nabla)\vec{v} - \nabla p + Pr\nabla^2 \vec{v} + \vec{F}]$. Since $\vec{v}$ is a divergence-free vector, we are led to get $P(\frac{\partial \vec{v}}{\partial t}) = \frac{\partial \vec{v}}{\partial t}$ or $\frac{\partial \vec{v}}{\partial t} = P(-(\vec{v} \cdot \nabla)\vec{v} - \nabla p + Pr\nabla^2 \vec{v} + \vec{F})$.

Following the concept of the orthogonal splitting of the equations described above, the vector field can be decomposed into the zero curl and the zero divergence parts. The intermediate velocity $\vec{v}^{n+\frac{1}{2}}$ for solving the problem subjected to the prescribed no-slip velocity can then be calculated from the following fully implicit equation, with the pressure variable being eliminated from the momentum equations

$$\frac{\vec{v}^{n+\frac{1}{2}} - \vec{v}^{n}}{\Delta t} = -\left(\vec{v}^{n+\frac{1}{2}} \cdot \nabla\right)\vec{v}^{n+\frac{1}{2}} + Pr\nabla^2 \vec{v}^{n+\frac{1}{2}} + \vec{F}^{n+\frac{1}{2}}. \tag{4}$$

The vector $\vec{v}^{n+\frac{1}{2}}$ can be further calculated sequentially from the advection and diffusion steps based on the Marchuk–Yanenko fractional-step method [11]. Use of this method enables us to separate the nonlinear convective term from the viscous term. The advection step given by $\frac{\vec{v}_a^{n+\frac{1}{2}} - \vec{v}^{n}}{\Delta t} + (\vec{v}^{n} \cdot \nabla)\vec{v}^{n} = 0$ and the diffusion step given by $\frac{\vec{v}^{n+\frac{1}{2}} - \vec{v}_a^{n+\frac{1}{2}}}{\Delta t} = Pr\nabla^2 \vec{v}^{n+\frac{1}{2}} + \vec{F}^{n+\frac{1}{2}}$ are resulted.

Note that the intermediate velocity solution $\vec{v}^{n+\frac{1}{2}}$ calculated from the above two steps does not necessarily satisfy the divergence-free constraint condition. As a result, the intermediate velocity $\vec{v}^{n+\frac{1}{2}}$ needs to be decomposed into the sum of the solenoidal velocity field $\vec{v}^{n+1}$ and the gradient of the currently chosen scalar function, which is proportional to $\Delta t\nabla p^{n+1}$. Our motivation of employing the projection step given by $\frac{\vec{v}^{n+1} - \vec{v}^{n+\frac{1}{2}}}{\Delta t} = -\nabla p^{n+1}$ and $\nabla \cdot \vec{v}^{n+1} = 0$ becomes enlightened. Calculation of the solution for $\vec{v}^{n+1}$ needs a pressure solution. The Poisson equation $\nabla^2 p = \nabla \cdot \vec{v}^{n+\frac{1}{2}}$ for the pressure can be therefore derived by virtue of $\nabla \cdot \vec{v}^{n+1} = 0$.

Based on the regularization method, the equation $\frac{\vec{v}^{n+1} - \vec{v}^{n+\frac{1}{2}}}{\Delta t} + \nabla p^{n+1} = 0$ is substituted into the semi-discrete momentum equation to get

$$\frac{\vec{v}^{n+1} - \vec{v}^{n}}{\Delta t} + \left(\vec{v}^{n+\frac{1}{2}} \cdot \nabla\right)\vec{v}^{n+\frac{1}{2}} - Pr\nabla^2 \vec{v}^{n+\frac{1}{2}} + \nabla p^{n+1} = M_1 + M_2 + \vec{F}^{n+1}, \tag{5}$$

where $M_1 = \left[\left(\vec{v}^{n+\frac{1}{2}} \cdot \nabla\right)\nabla p^{n+1} + (\nabla p^{n+1} \cdot \nabla)\vec{v}^{n+\frac{1}{2}} - Pr\nabla^2(\nabla p^{n+1})\right]\Delta t$ and $M_2 = -[(\nabla p^{n+1} \cdot \nabla)\nabla p^{n+1}]\Delta t^2$. Let $p^{n+1} = p^* + p'$, the pressure-gradient step is decomposed into $\frac{\vec{v}^* - \vec{v}^{n+\frac{1}{2}}}{\Delta t} = -\nabla p^*$ and $\frac{\vec{v}^{n+1} - \vec{v}^*}{\Delta t} = -\nabla p'$, where p^* denotes the intermediately predicted pressure. Eq. (5) can be therefore reformulated as

$$\frac{\vec{v}^{n+1} - \vec{v}^{n}}{\Delta t} + (\vec{v}^* \cdot \nabla)\vec{v}^* - Pr\nabla^2 \vec{v}^* + \nabla p^* = -\nabla p' + M_3 + M_4 + \vec{F}^{n+1}. \tag{6}$$

In the above, $M_3 = [(\vec{v}^* \cdot \nabla)\nabla p' + (\nabla p' \cdot \nabla)\vec{v}^*]\Delta t - Pr\nabla(\nabla \cdot \vec{v}^*)$ and $M_4 = -[(\nabla p' \cdot \nabla)\nabla p']\Delta t^2$. Given the predicted values for $\vec{v}_0^*$ and p_0', the employed algorithm is summarized below for completeness.

For $s = 1, 2, \ldots$

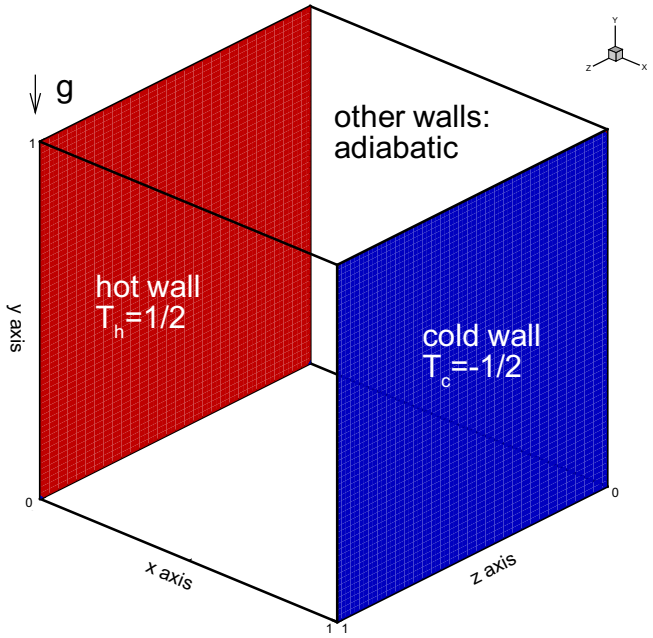

Fig. 1. Schematic of the investigated thermally driven cavity.

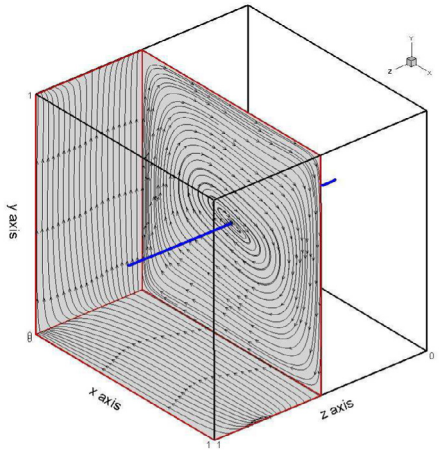

(a) single cell flow structure (2.8×10^4)

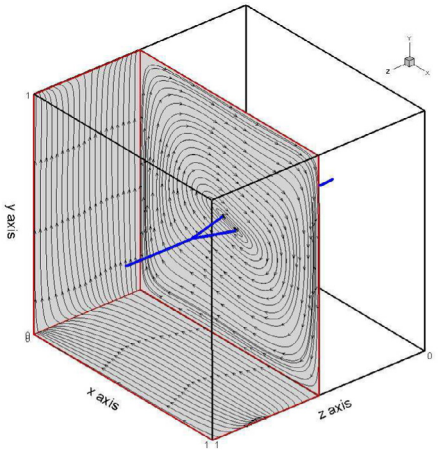

(b) double fork-type cell flow structure (2.9×10^4)

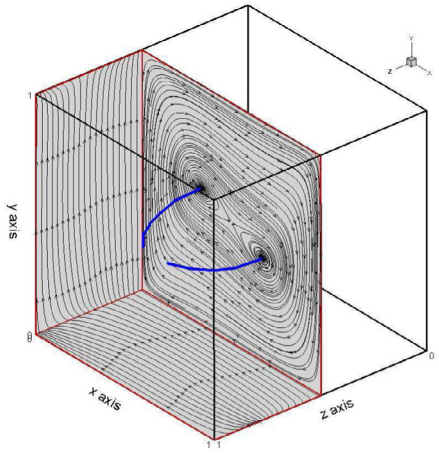

(c) 2-cell flow structure (5.4×10^4)

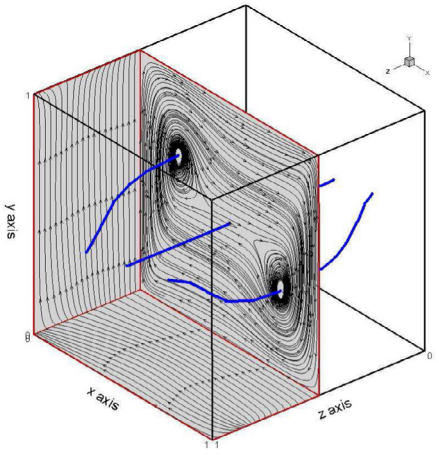

(d) 3-cell flow structure (2.9×10^5)

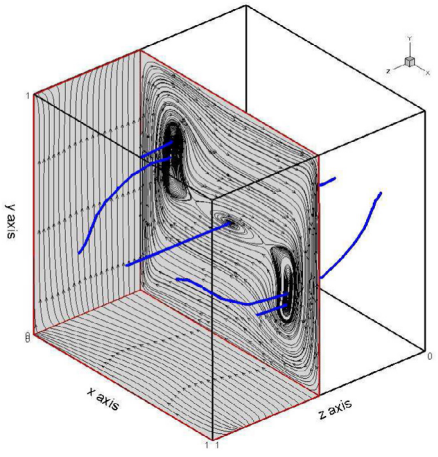

(e) 5-cell flow structure (6.1×10^5)

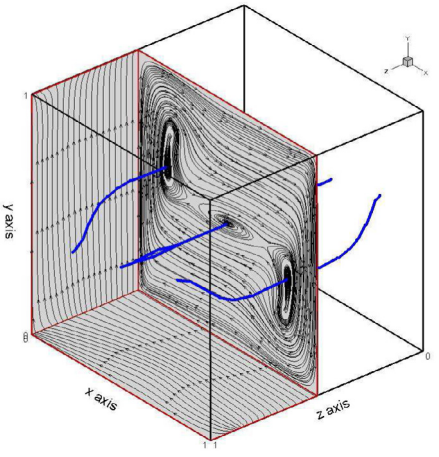

(f) 3-cell flow structure (7.3×10^5)

Fig. 2. The predicted time-evolving flow structures which are exhibited by the plotted vortical corelines and the limiting streamlines on the two half planes ($x = 0.001$), ($y = 0.001$), and the streamlines on the center plane $z = 0.5$.

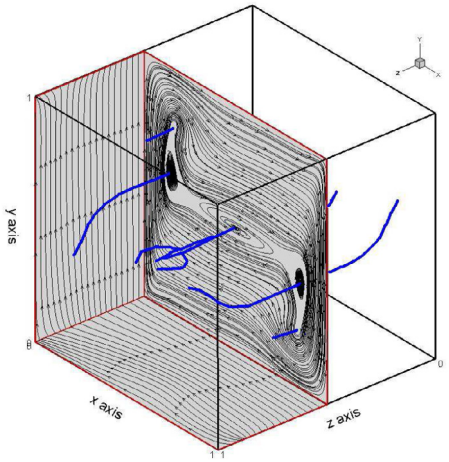

(g) 5-cell flow structure (1.2×10^6)

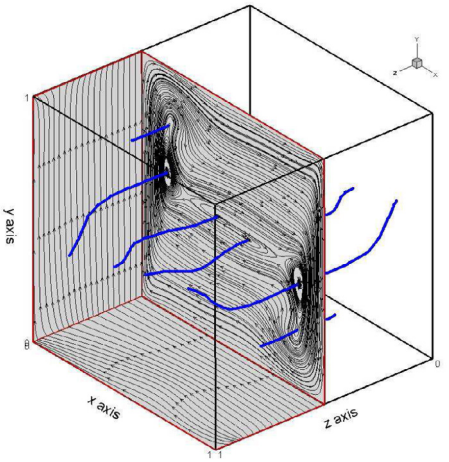

(h) 6-cell flow structure (1.5×10^6)

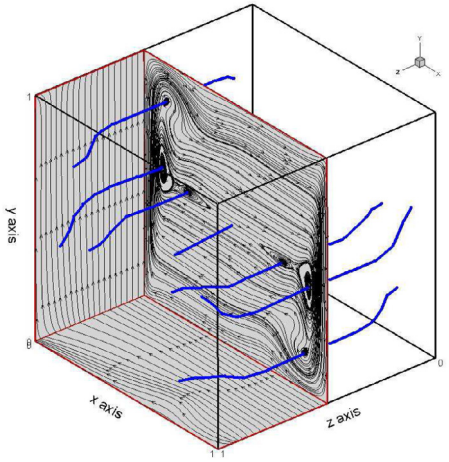

(i) 7-cell flow structure (6.5×10^6)

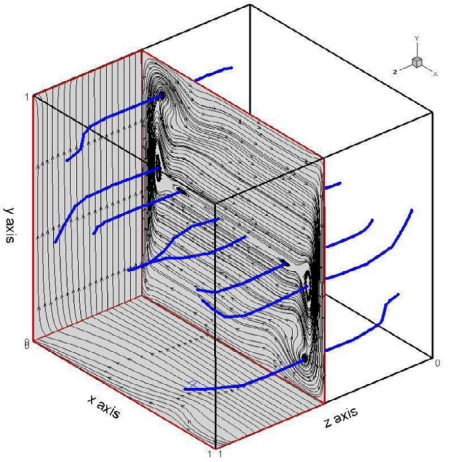

(j) 8-cell flow structure (1.3×10^7)

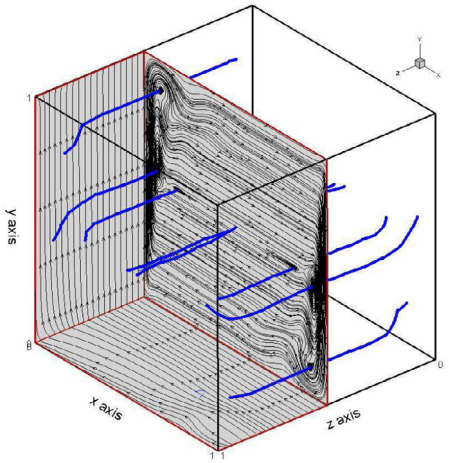

(k) 7-cell flow structure (3×10^7)

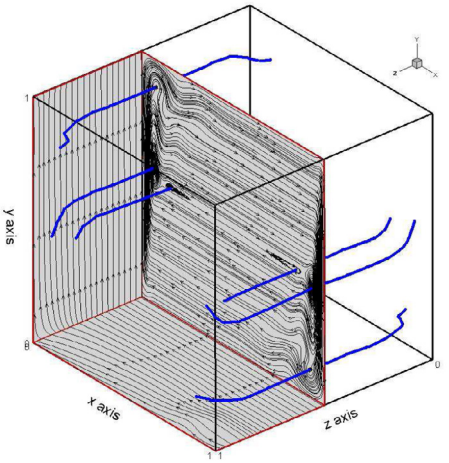

(l) 6-cell flow structure (5.4×10^7)

Fig. 2 (*continued*)

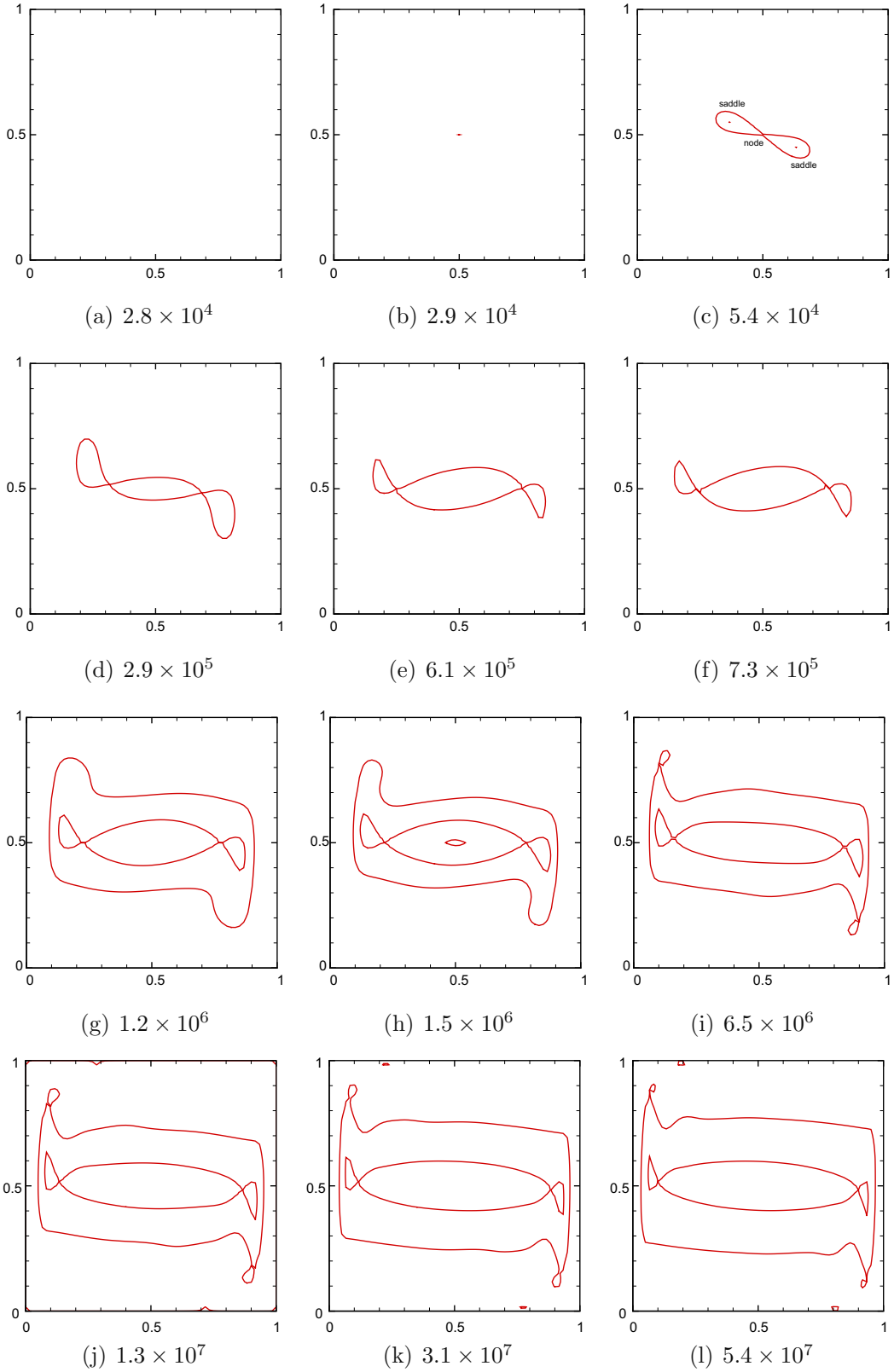

Fig. 3. Plots of the zero streamline contours and the simulated nodes *N* and saddles *S* on the plane of symmetry $z = 0.5$ for the cases investigated at different Rayleigh numbers shown in Fig. 2.

cell number	flow interior	around the corner	Rayleigh number	Figure number
1	N		2.8×10^4	2(a)
2*	N		2.9×10^4	2(b)
2	N-S-N		5.4×10^4	2(c)
3	N-S-N-S-N		2.9×10^5	2(d)
5*	N-S-N-S-N	S-N, S-N	6.1×10^5	2(e)
3*	N-S-N-S-N		7.3×10^5	2(f)
5	N-S-N-S-N	S-N, S-N	1.2×10^6	2(g)
6	N-S-N-S-N-S-N	S-N, S-N	1.5×10^6	2(h)
7	N-S-N-S-N-S-N-S-N	S-N, S-N	6.5×10^6	2(i)
8	N-S-N-S-N-S-N-S-N-S-N	S-N, S-N	1.3×10^7	2(j)
7*	N-S-N-S-N-S-N-S-N	S-N, S-N	3.1×10^7	2(k)
6	N-S-N-S-N-S-N	S-N, S-N	5.4×10^7	2(l)

(a)

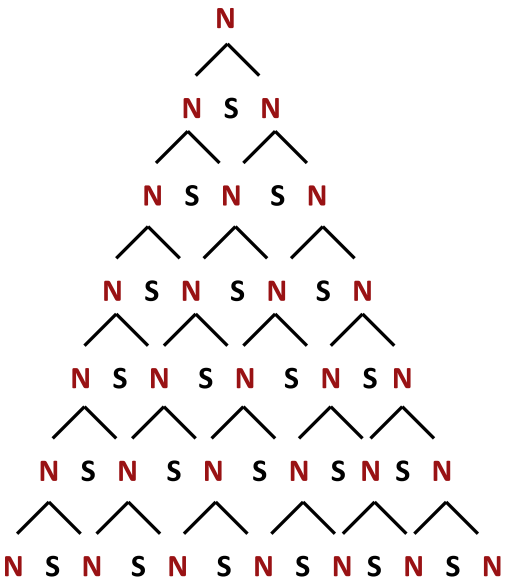

(b)

Fig. 4. Classification of the predicted time-evolving cellular flow structures. (a) saddle-node pairs; (b) formation sequence of the critical points.

$$\frac{\vec{v}_s^{n+1}-\vec{v}^n}{\Delta t}+\vec{v}_s^*\cdot\nabla\vec{v}_s^*-Pr\,\nabla^2\vec{v}_s^*+\nabla p_{s-1}^*=-\nabla p_{s-1}'+\vec{F}^{n+1}, \tag{7}$$

$$p_s^*=p_{s-1}^*+p_s', \tag{8}$$

$$\vec{v}_{s+1}^*=\vec{v}_s^{n+1}-\Delta t\nabla p_s'. \tag{9}$$

The equation for p' is derived by performing the divergence operator on $\frac{\vec{v}^{n+1}-\vec{v}^*}{\Delta t}=-\nabla p^*$ to get $\nabla^2 p'=\frac{\nabla\cdot\vec{v}^*}{\Delta t}$. At an interior point (i,j), the following centered scheme is applied to approximate the Poisson equation for p', thereby yielding the following equation for $p'_{i,j}$

$$2\left(\frac{1}{\Delta x^2}+\frac{1}{\Delta y^2}\right)p'_{i,j}=\frac{\nabla\cdot\vec{v}^*}{\Delta t}-\frac{1}{\Delta x^2}\left(p'_{i-1,j}+p'_{i+1,j}\right)-\frac{1}{\Delta y^2}\left(p'_{i,j-1}+p'_{i,j+1}\right). \tag{10}$$

By omitting the term $\frac{1}{\Delta x^2}(p'_{i-1,j}+p'_{i+1,j})+\frac{1}{\Delta y^2}(p'_{i,j-1}+p'_{i,j+1})$, the equation for the pressure correction can be derived as

$$p'_{i,j}=-\frac{\Delta x^2\Delta y^2}{2(\Delta x^2+\Delta y^2)\Delta t}\,\nabla\cdot\vec{v}^*. \tag{11}$$

The above derived pressure correction equation may over-determine the pressure solution due to the omitted term. To compensate for this omission, Eq. (11) is employed to calculate the pressure correction term p'^*. This is followed by calculating p' from p'^* as

$$p'_{i,j}=p'^*_{i,j}+\frac{\Delta y^2}{2(\Delta x^2+\Delta y^2)}\left(p'^*_{i-1,j}+p'^*_{i+1,j}\right)+\frac{\Delta x^2}{2(\Delta x^2+\Delta y^2)}\left(p'^*_{i,j-1}+p'^*_{i,j+1}\right). \tag{12}$$

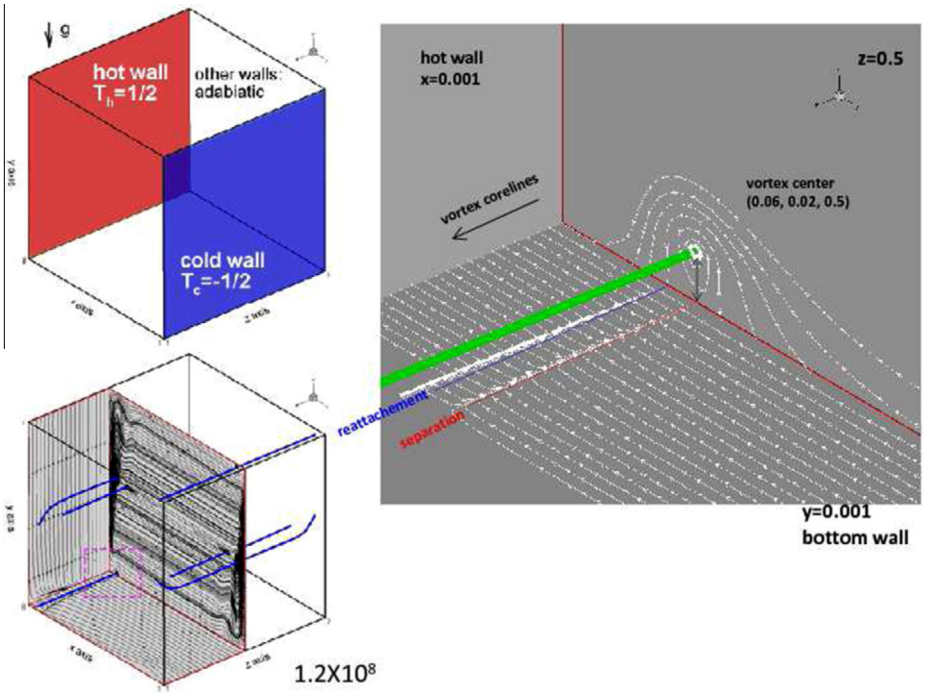

Fig. 5. Illustration of the simulated lines of separation/reattachment in the cavity corner near the vertical heated wall.

While even–odd pressure oscillations can be well eliminated by the method formulated in staggered grids, in this study the gradient term for the pressure (or ∇p) is approximated in a programmingly more simple non-staggered (or collocated) mesh to avoid spurious pressure oscillations. Taking the nodal value of p_j at an interior node j as an example, the approximated value of p_x (*or* $F_j\ (\equiv h\, p_x|_j)$) can be calculated from the following implicit equation

$$\gamma_1 F_{j+1} + \gamma_2 F_j + \gamma_3 F_{j-1} = c_1(p_{j+2} - p_{j+1}) + c_2(p_{j+1} - p_j) + c_3(p_j - p_{j-1}) + c_4(p_{j-1} - p_{j-2}). \quad (13)$$

Note that h denotes the constant grid spacing. The readers can refer to Sheu & Lin [12] for the determination of γ_1 to γ_3 and c_1 to c_5.

When simulating high Reynolds number flows, it is essential to apply a dispersively more accurate advection scheme. The same upwinding scheme proposed in [13] is applied to get the advection scheme with the optimized modified wavenumber for the advective terms $\frac{\partial \vec{u}}{\partial \vec{x}}$, where $\vec{u} = (u, v, w)$ and $\vec{x} = (x, y, z)$. This scheme is derived by applying the modified equation analysis and the method of minimizing the difference between the exact and numerical modified wavenumbers.

The grid-independent velocity profiles $u(x, \frac{1}{2}, z)$, $v(\frac{1}{2}, y, z)$ and $T(\frac{1}{2}, y, z)$ predicted at $Ra = 10^6$ and $Pr = 0.71$ have been compared with other available numerical results with good agreement in the currently investigated cube [13]. The dimensionless Nusselt numbers have also been compared with good agreement with those in the above paper.

4. Numerical results

A Boussinesq fluid flow is investigated at the Prandtl number Pr (=0.71) in a cube $(0 \leqslant x, y, z \leqslant 1)$. In the current simulation, all the six wall boundaries schematic as shown in Fig. 1 are prescribed by the no-slip condition for $\underline{u}$ (*or* $\underline{u} = 0$) while solving the Eqs. (1) and (2). For the closure of the energy Eq. (3), these cavity walls are assumed to be thermally insulated or $\frac{\partial T}{\partial \vec{n}} = 0$ at $(x, y = 0, 1, z)$ and $(x, y, z = 0, 1)$, where $\vec{n}$ is the unit normal derivative, except at the two isothermal vertical walls. The left vertical wall located at $x = 0$ is a heated wall $(T_h = \frac{1}{2})$ and the right one at $x = 1$ is a cold wall $(T_c = -\frac{1}{2})$.

4.1. Evolution of different cellular flow patterns

At the Rayleigh number $Ra = 2.8 \times 10^4$, a single-cell flow pattern was stationarily developed in the cavity. Such a flowfield is featured to have one spiraling node "*N*" shown in Fig. 2(a), which plots the streamlines at the central plane. A span of these spiraling nodes at each cutting plane along x direction yields the so-called vortical coreline, thus illustrating the signature of the vortical flowfield.

By increasing the Rayleigh number to 2.9×10^4, the above mentioned one-cell flowfield can no longer be retained because of the increased nonlinearity. The thermally driven cavity flow becomes exhibiting a double fork-type vortical flow pattern and the resulting vortical flowfield has been divided into two main regions. One region has a single vortical flow pattern and the other region contains two counter-rotating vortical flows shown in Fig. 2(b). As the Rayleigh number keeps increasing to $Ra = 5.4 \times 10^4$, the single cellular flow pattern formerly existing in the cavity disappears and the flow has been split into two cells with the birth of a new saddle point "*S*" located between the two spiraling nodes "*N*" schematic as shown in Fig. 2(c). With a continuous increase of the value of Ra to 2.9×10^5, the flowfield with two apparent vortical corelines evolves to exhibit a new flow pattern marked by the three vortical-corelines shown in Fig. 2(d). Such a three-coreline vortical flow is accompanied with the formation of a new set of "*N*" and "*S*" topological points, thereby leading to a *N-S-N-S-N* critical-point pattern. As the Rayleigh number becomes as large as 6.1×10^5, two additional spiraling nodes plotted in Fig. 2(e) make their first appearance near the cavity corner.

The critical points displayed in a *N-S-N-S-N-S-N-S-N* form with the *N-S* and *S-N* pairs in the cavity corners is a direct consequence of the increased Rayleigh number. It is interesting to find from Fig. 2(f) that the number of critical points in the form of *N-S-N-S-N*

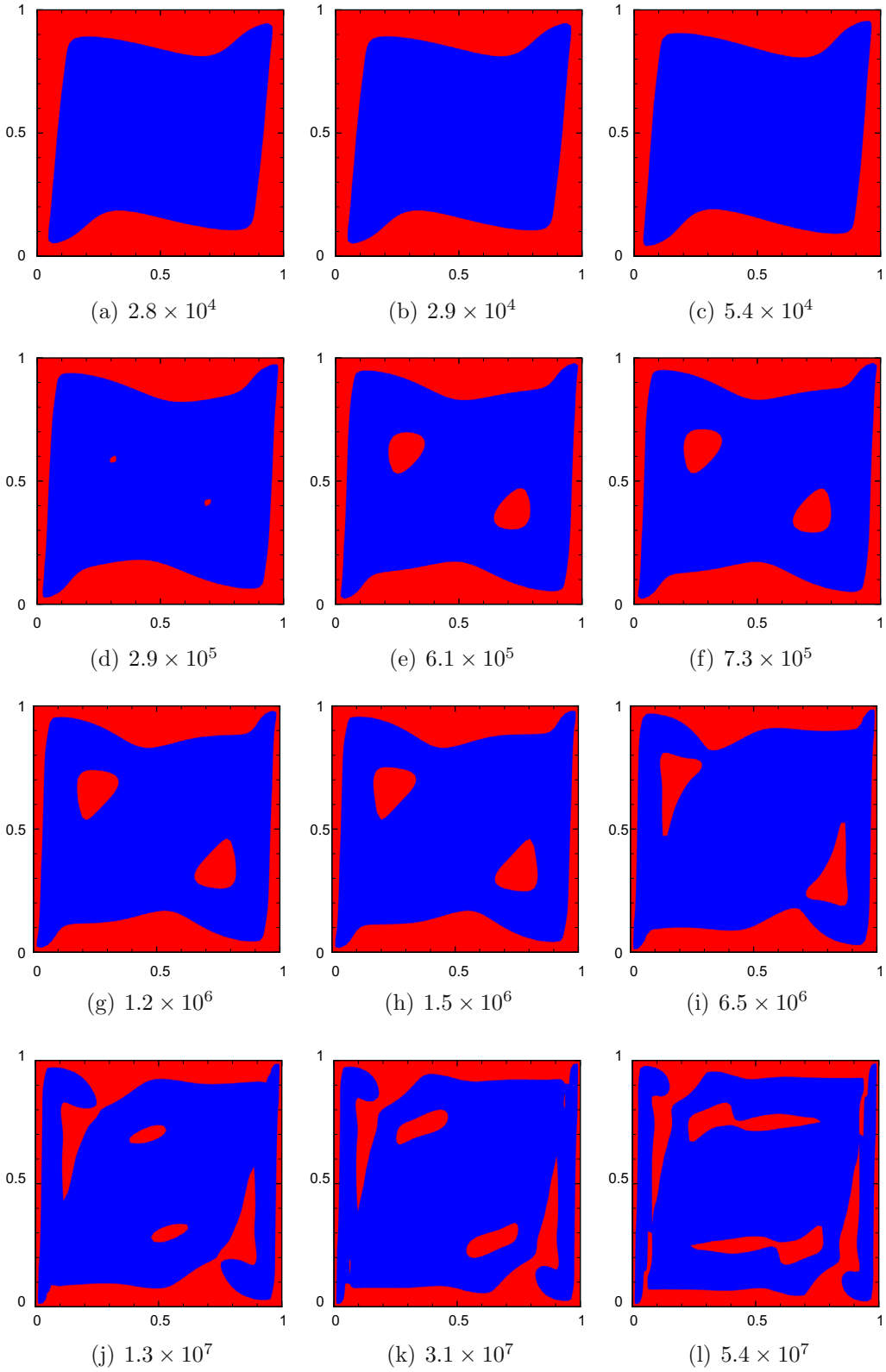

Fig. 6. Plots of the zero vorticity lines, which are the lines between the positive-valued vorticity (marked with red-colored region) and the negative-valued vorticity (marked with blue-colored region) for the cases investigated at different Rayleigh numbers. Note that vorticity is defined by $\underline{\omega} = \nabla \times \underline{u}$. (For interpretation of the references to colour in this figure caption, the reader is referred to the web version of this article.)

is surprisingly reduced as the Rayleigh number is increased to $Ra = 7.3 \times 10^5$. With a further increment in Ra to 1.2×10^6, the cavity flow with three vortical corelines is found to increase again the number of corelines by two. The five predicted corelines are shown in Fig. 2(g), with the four saddles "S" lying between the two adjacent nodes "N". At $Re = 1.5 \times 10^6$, one extra saddle-node pair shown in

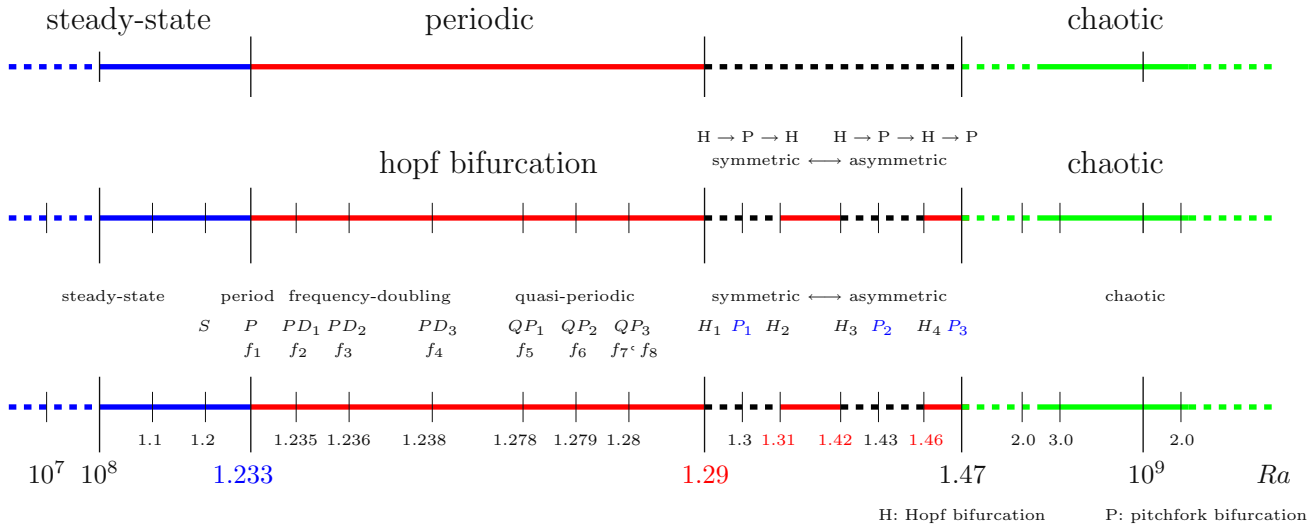

Fig. 7. A complete bifurcation diagram and the predicted critical *Ra* values. The solid and dashed lines denote the symmetric and asymmetric flow behaviors, respectively.

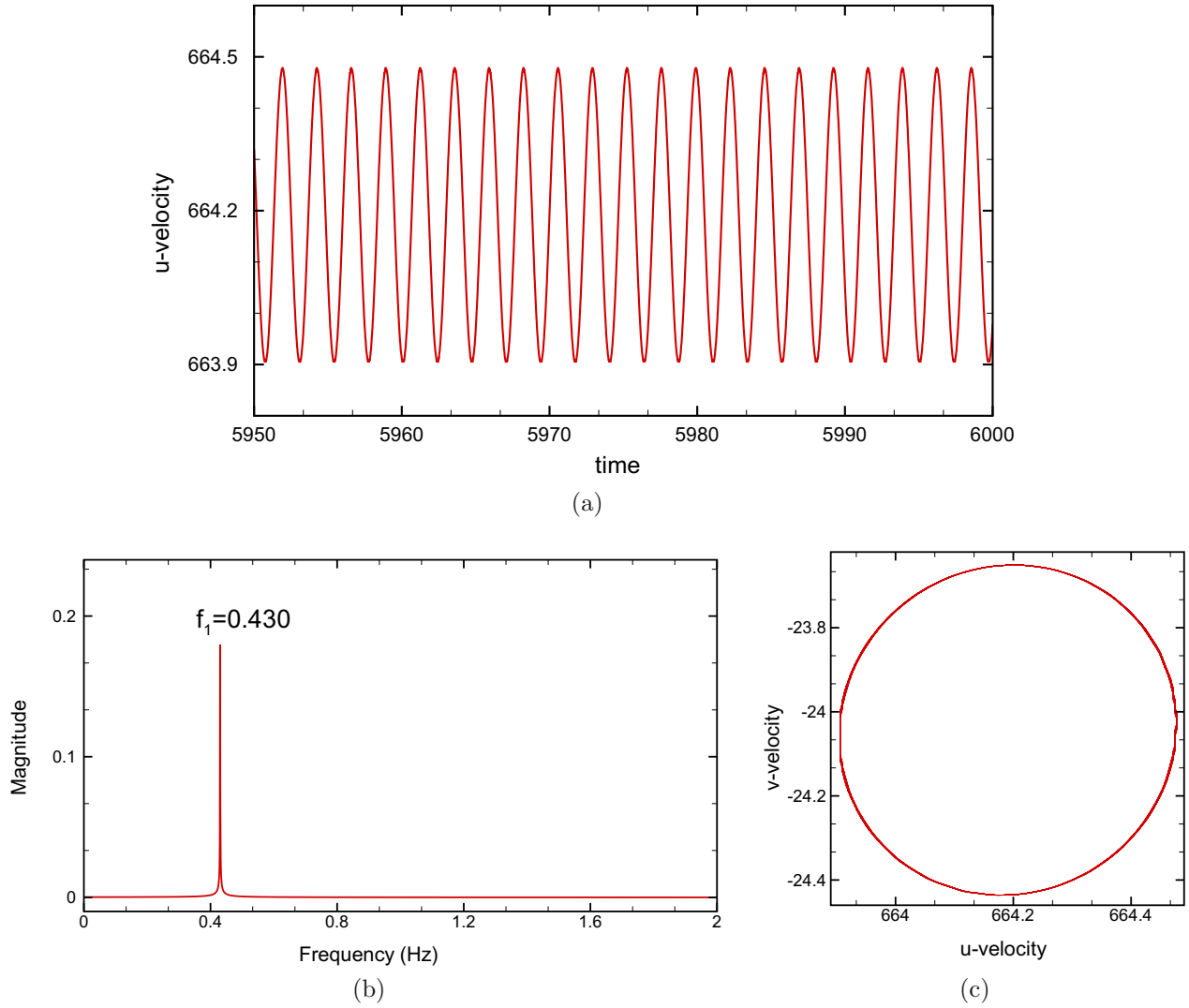

Fig. 8. The power spectrum of the predicted *u*-velocity component at the chosen point $(x, y, z) = (0.9, 0.9, 0.9)$, where the primary frequency is $f_1 \approx 0.430$ Hz, for the case investigated at $Ra_P = 1.233 \times 10^8$. (a) Time-evolving *x*-component velocity *u*; (b) FFT plot; (c) limit cycle.

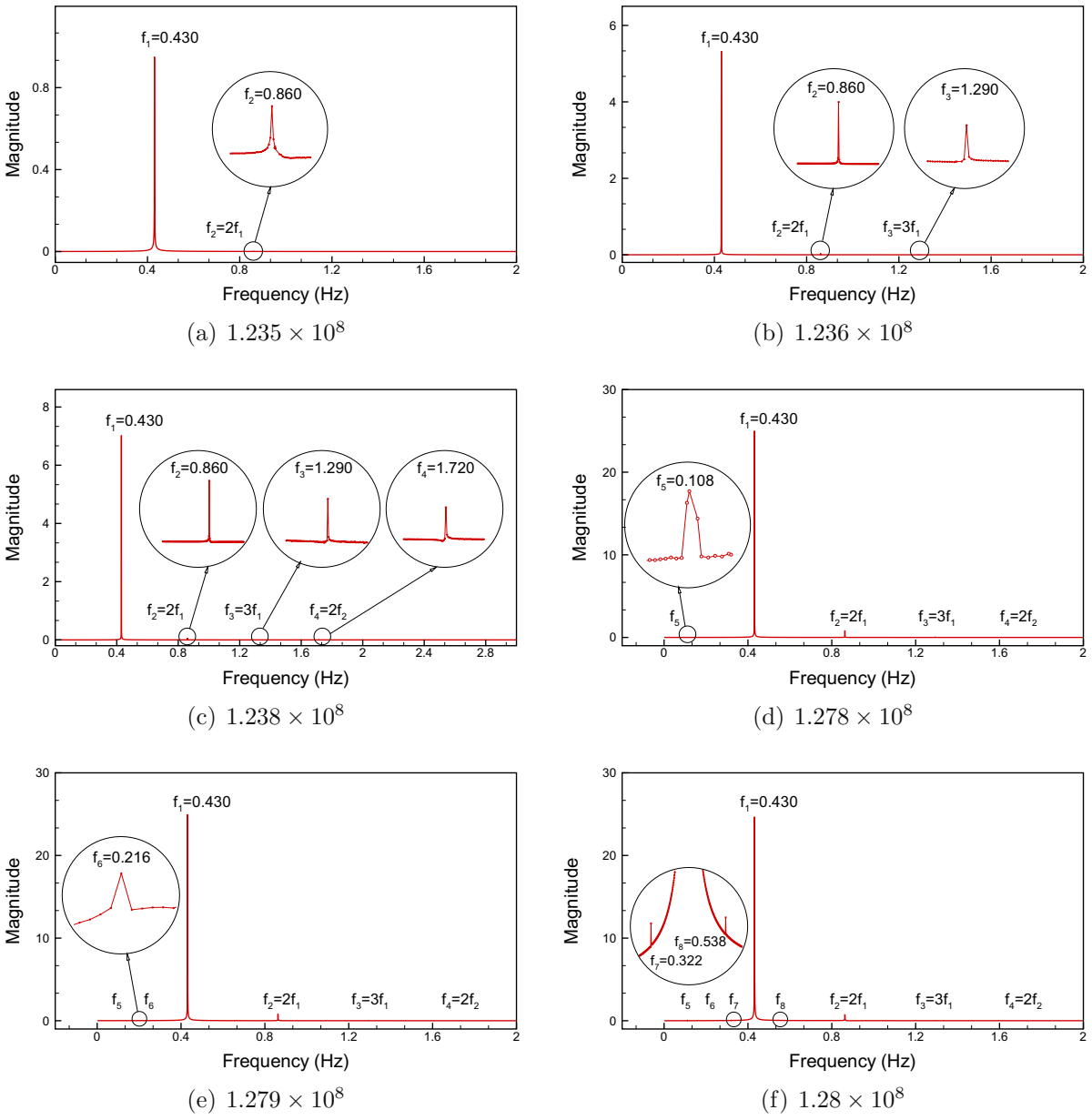

Fig. 9. The power spectrum of the predicted u-velocity component at the chosen point $(x, y, z) = (0.9, 0.9, 0.9)$, where $f_1 \approx 0.430$ Hz, $f_2 = 2f_1, f_3 = f_1 + f_2, f_4 = 2f_2, f_5 \approx 0.108$ Hz, $f_6 = 2f_5 \approx 0.216$ Hz, $f_7 = f_1 - f_5$ and $f_8 = f_1 + f_5$.

Fig. 2(h) constitutes the flow having a total number of six vortical corelines. The number of vortical corelines will keep increasing respectively to seven and eight, as shown in Figs. 2(i) and (j), respectively, at $Ra = 6.5 \times 10^6$ and 1.3×10^7.

For the sake of clearness, the topologically singular points (nodes N and saddles S) are plotted in the plane of symmetry at $z = 0$, on which the streamline contours of zero magnitude are plotted in Fig. 3 for the cases considered at different Rayleigh numbers. The number of the predicted vortical corelines and their corresponding critical points are summarized as shown in Fig. 4 for the flow investigated in the range of $Ra \leqslant 6 \times 10^6$.

When increasing the value of Ra, it is interesting to find that the reduction of the number of vortical corelines at $Ra = 1.18 \times 10^8$ is in accompany with the formation of two pairs of the separation-and-reattachment lines, as shown in Fig. 5, on the walls $z = 0$ and $y = 0$. We also plot the zero vorticity contour lines, between the positive vorticity region (marked by red color) and the negative vorticity region (marked by blue color) in Fig. 6, on the symmetry plane $z = 0$. These contour plots reveal the link between the predicted topologically singular points (nodes and saddles) and the vortical flow directions.

4.2. Pitchfork bifurcation

Bifurcation types frequently found in nonlinear dynamical systems include the pitchfork (symmetry-breaking), transcritical, saddle-node (or tangent, or blue sky), Hopf, flip, Niemark (or secondary Hopf), homoclinic, period-doubling, and catastrophic bifurcations. Our attention of this study is paid exclusively to the formation of pitchfork bifurcation in the buoyancy driven flow. Hopf and pseudo-periodic bifurcations predicted in the currently investigated cavity have been discussed in detail in our previous paper [13]. They will be briefly summarized again in Section 4.3 for the sake of completeness.

For a nonlinear system subjected to a perturbation in the investigated geometrically symmetric cavity, pitchfork bifurcation will

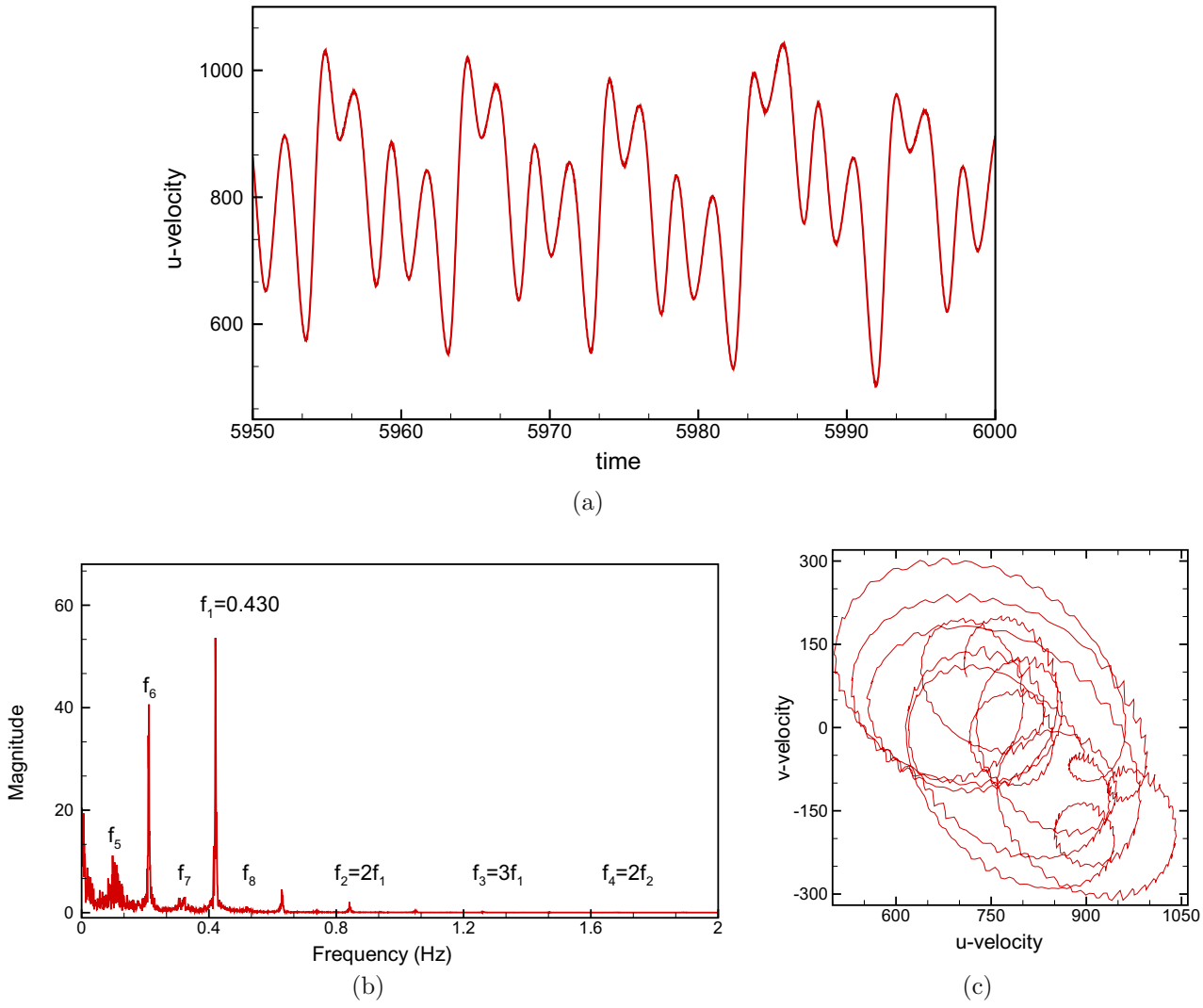

Fig. 10. The power spectrum of the predicted u-velocity component at the chosen point $(x,y,z) = (0.9, 0.9, 0.9)$, where $f_1 \approx 0.430$ Hz, $f_2 = 2f_1, f_3 = f_1 + f_2, f_4 = 2f_2, f_5 \approx 0.108$ Hz, $f_6 = 2f_5 \approx 0.216$ Hz, $f_7 = f_1 - f_5$ and $f_8 = f_1 + f_5$, for the case investigated at $Ra = 1.3 \times 10^8$. (a) Time-evolving x-component velocity u; (b) FFT plot; (c) limit cycle.

Table 1
The predicted route to chaos.

Route to chaos	Periodic (P)	Periodic (PD_1)	Periodic (PD_2)	Periodic (FD_3)	Quasi periodic (QP_1)	Quasi periodic (QP_2)	Quasi periodic (QP_3)	Chaotic (C)
Critical Ra	1.233×10^8	1.235×10^8	1.236×10^8	1.238×10^8	1.278×10^8	1.279×10^8	1.28×10^8	1.5×10^8
Number of peak frequencies	1	2	3	4	4	5	8	–

occur as the control parameter Ra exceeds its critical value. As the solution bifurcates, its corresponding eigenvalue of the fixed point reaches 1. The resulting geometrically symmetric flow becomes destabilized with the breaking of flow symmetry. Hence pitchfork bifurcation solution is also called as the symmetry-breaking solution. When pitchfork bifurcation sets in, the solution in the stable branch becomes unstable with the formation of two newly born stable branches.

The L_2-error norms for $(\vec{v}, p)$ and the heat flux were calculated in the regions with the plane of symmetry versus the values of Ra to clearly illustrate the evolution of pitchfork bifurcation along the $y = 0.5$ plane in the range of $10^3 \leqslant Ra \leq 1.5 \times 10^8$. Initially, for $Ra \leqslant 10^3$ the L_2-error norm was very close to zero. This implies that the flow was symmetric with respect to the plane $y = 0.5$ for $Ra \leq 1.29 \times 10^8$, which is the first critical pitchfork bifurcation value $Ra(Ra_{CP_1})$. As Ra is increased beyond this critical value, the L_2-error norms were seen to become larger than zero, implying the initiation of pitchfork bifurcation. When the value of Ra was increased further to 1.3×10^8, the predicted L_2-error norms were found to be very close to zero again and the flow becomes symmetric. When the Rayleigh number is increased by a small amount to $Ra = 1.42 \times 10^8$, the flow is seen to switch from the symmetric steady-state to the asymmetric steady-state. The exhibited asymmetric solution indicates the presence of the second pitchfork bifurcation. As Ra becomes larger than 1.43×10^8, the buoyancy driven flow no longer shows the unsymmetric nature.

A complete evolution of the solution branches is shown schematically by presenting the global pitchfork bifurcation diagram

(Fig. 7) with respect to the Rayleigh numbers at $y = 0.5$ plane. The first bifurcation occurring at $Ra = 1.29 \times 10^8$ is responsible for the flow transition from the symmetric steady-state solution to its unsymmetric counterpart. The other two critical values, namely, $Ra_{CP_2} = 1.42 \times 10^8$, lead respectively to the second pitchfork bifurcation.

4.3. Other bifurcations predicted in the nonlinear system

In Fig. 8, the predicted phase portrait and power spectrum, which displays the power versus the frequency, show that the flow is strictly periodic with the fundamental frequency $f_1 = 0.42998394$ at $Ra = 1.233 \times 10^8$. By increasing the Rayleigh number from 1.233×10^8 by a small amount to 1.235×10^8, in Fig. 9(a) an additional extraharmonics with the frequency that doubles the fundamental frequency can be observed. This bifurcation is called as the frequency-doubling bifurcation (FD_1) because of the existence of two commensurate frequencies, namely, $f_1 = 0.42998394$ and $f_2 = 2f_1 = 0.85996789$. Many other commensurate frequencies with much smaller values of the power can be found in Figs. 9(b) and (c) as the Rayleigh numbers are slightly increased. Note that the interval of Ra becomes shorter and shorter with the increased peak frequency in the sense that the second and third additional ultraharmonic frequencies, which are defined as mf_1/n for $n = 1$ and $m = 1, 2, 3\ldots$[14], were found respectively at $Ra = 1.236 \times 10^8$ (for $m = 3$) and 1.238×10^8 (for $m = 4$). Note that all the predicted ultraharmonic frequencies are integer multiplies of the fundamental harmonic frequency f_1.

As the value of Ra was increased to 1.278×10^8, one can see in Fig. 9(d) a secondary frequency $f_5 (= 0.108\,\text{Hz})$. This implies that the thermally-driven flow system has been split into two families of the frequencies f_1 and f_5 as shown in Fig. 9(e) and (f). The second frequency f_5 is referred to as the subharmonic frequency. At this moment, flow becomes quasi-periodic with two fundamental frequencies f_1 and f_5 that are incommensurate to each other. In the eight predicted peak frequencies, they are related to each other arithmetically ($f_1 = 0.42998394, f_2 = 2f_1, f_3 = f_1 + f_2, f_4 = 2f_2$ and $f_5 \approx 0.108, f_6 = 2f_5, f_7 = f_1 - f_5$ and $f_8 = f_1 + f_5$). Although other frequencies may appear as well in the power spectrum, their amplitudes were several orders smaller than the amplitude of the primary frequency f_1. In the presence of the predicted frequency f_5, which is incommensurate to frequencies f_1 to f_4, the flow is no longer periodic. The investigated nonlinear dynamical system has proceeded a quasi-periodic route to chaos.

By continuously increasing the Rayleigh number, more and more fundamental frequencies are observed. The path of the solution can no longer be repeated and chaos sets in. Fig. 10 shows the onset of chaotic flow at the $Ra = 1.3 \times 10^8$. The power spectrum for the disorganized solutions has a rich spectral structure. Such a broad-band power spectrum hints the existence of a continuous frequency pattern. The route to chaos is summarized in Table 1.

5. Conclusions

Nonlinear, natural convective, thermally driven flow inside a cube with the high and low temperatures prescribed at two opposing vertical walls is studied here numerically. Through this 3D numerical study, prior to $Ra = 2.8 \times 10^4$ the thermally driven flow in the cube is known to remain steady with a single vortical coreline of a symmetric vortex type. At $Ra = 2.9 \times 10^4$, the single-cell flowfield is evolved to exhibit a double fork-type vortical flow pattern. Saddle point appears in the core of the cavity between two symmetric topological nodes at $Ra = 5.4 \times 10^4$, thereby forming a pair of counter-rotating cellular flow field. With the increase of Rayleigh number, the formation of two new sets of the node-and-saddle pair yields the *N-S-N-S-N* and, then, the *N-S-N-S-N-SN-SN* patterns of the critical points. It is surprising to find the reduced number of the interior critical points to five and three as the value of Ra has been increased to 7.3×10^5 and 1.2×10^6, respectively. Afterwards, the numbers of vortical corelines increase to seven and eight at $Ra = 6.5 \times 10^8$ and 1.3×10^7, respectively. Flow was predicted to lose stability by firstly exhibiting flow asymmetry at $Ra = 1.29 \times 10^8$. This is followed to form the other pitchfork bifurcation at $Ra = 1.42 \times 10^8$. The solution predicted at $Ra_{CH_1} = 1.233 \times 10^8$ was seen to transit from the stationary to the time-periodic states. As the value of Ra exceeds 1.233×10^8, the growth of 3-D nonlinear effects in the flow could generate more ultraharmonic frequencies. The secondary Hopf bifurcation was seen to appear approximately at $Ra = 1.278 \times 10^8$. The appearance of such a subharmonic frequency, which is incommensurate to the primary harmonic frequency, and its ultraharmonic frequencies leads altogether to the quasi-periodic flow. At higher values of Ra, eight arithmetically related fundamental frequencies are seen in the two fundamental frequency families and, then, the sequence of infinite frequencies was observed. Ultimately, the thermally driven flow was evolved to show corrugated torus and strange attractor. The chaotic flow was then observed at $Ra = 1.6 \times 10^8$.

Conflict of interest

None declared.

Acknowledgments

The financial support provided by the (Taiwan) Ministry of Science and Technology under Grant MOST102-2221-E-229-001 is gratefully acknowledged. The authors also thank the Computer Center of National Taiwan University and the National Center of High-performance Computing (NCHC) for providing us the requested computing resources.

References

[1] L. Rayleigh, On convection currents in a horizontal layer of fluid, when the higher temperature is on the under side, Philos. Mag. (1916) 529–546.
[2] S. Chandrasekhar, Hydrodynamic and Hydromagnetic Stability, Dover Publications. Inc., 1981.
[3] P. Drazin, W. Reid, Hydrodynamic Stability, Cambridge University Press, 1981.
[4] K. Kirchgäsner, Bifurcation in nonlinear hydrodynamic stability, SIAM Rev. 17 (1975) 652–683.
[5] V.I. Yudovich, Free convection and bifurcation, J. Appl. Math. Mech. 31 (1967) 103–114.
[6] A.Yu. Gelfgat, P.Z. Bar-Yoseph, A.L. Yarin, Stability of multiple steady states of convection in laterally heated cavities, J. Fluid Mech. 388 (1999) 315–334.
[7] L. Quartapelle, M. Napolitano, Integral conditions for the pressure in the computation of incompressible viscous flows, J. Comput. Phys. 64 (1986) 340–348.
[8] S.F. Tsai, T.W.H. Sheu, Finite-element analysis of incompressible Navier–Stokes equations involving exit pressure boundary conditions, Numer. Heat Transfer, B Fundam. 39 (5) (2001) 479–507.
[9] T.W.H. Sheu, S.F. Tsai, M.T. Wang, Discussion of numerical deficiency of applying a partially weighted upwind finite-element model to incompressible Navier–Stokes equations, Numer. Heat Transfer, B Fundam. 32 (2) (1997) 197–214.
[10] O.A. Ladyzhenskaya, The Mathematical Theory of Viscous Incompressible Flow, Gordon and Breach, New York, 1969.
[11] G.I. Marchuk, Methods of Numerical Mathematics, Springer, New York, 1975.
[12] T.W.H. Sheu, R.K. Lin, An incompressible Navier–Stokes model implemented on nonstaggered grids, Numer. Heat Transfer B Fundam. 44 (3) (2003) 277–294.
[13] T.W.H. Sheu, R.K. Lin, Three-dimensional bifurcations in a cubic cavity due to buoyancy-driven natural convection, Int. J. Heat Mass Transfer 54 (2011) 447–467.
[14] R. Enns, G. McGuire, Nonlinear Physics with Mathematica for Scientists and Engineers, Birhkauser, Boston, 2011.